

Supporting Information

Artificial Intelligence-Accelerated High-Throughput Screening of Antibiotic Combinations on a Microfluidic Combinatorial Droplet System

Deyu Yang^{a,+}, Ziming Yu^{a,+}, Mengxin Zheng^a, Wei Yang^a, Zhangcai Liu^a, Jianhua Zhou^{a,b,}, Lu Huang^{a,b*}*

^a School of Biomedical Engineering, Sun Yat-sen University, Shenzhen 518107, China

^b Key Laboratory of Sensing Technology and Biomedical Instruments of Guangdong Province, School of Biomedical Engineering, Sun Yat-sen University, Guangzhou 510275, China

*Corresponding author at: School of Biomedical Engineering, Sun Yat-sen University, Shenzhen 518107, China.

E-mail address: zhoujh33@mail.sysu.edu.cn (J. Zhou); huanglu39@mail.sysu.edu.cn (L. Huang).

Supporting Figures



Figure S1. A representative photograph of the modified droplet collection chip. Scale bar: 20 mm.

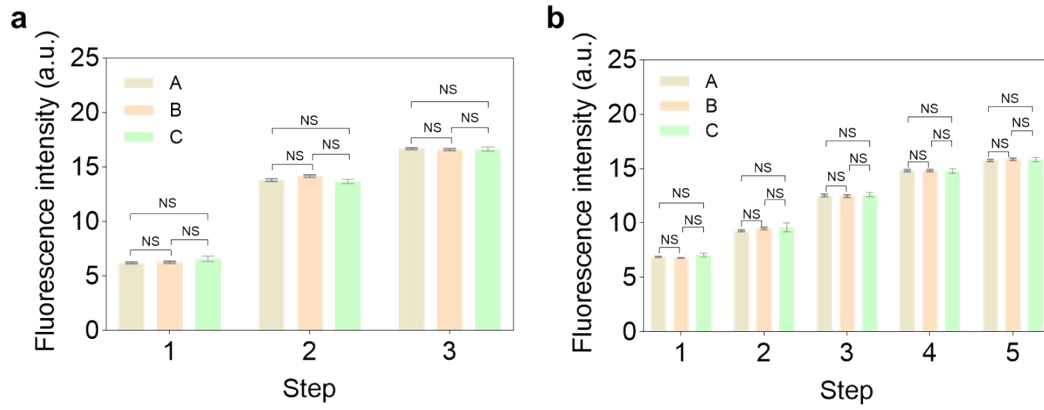


Figure S2. The average fluorescence intensity of all droplets generated at each step, all droplets except for the first 20 ones generated at each step, and droplets selected using our approach generated at each step under the 3-stepped (a) and 5-stepped (b) loading schemes. * $P < 0.05$, ** $P < 0.01$, *** $P < 0.001$ and **** $P < 0.0001$.

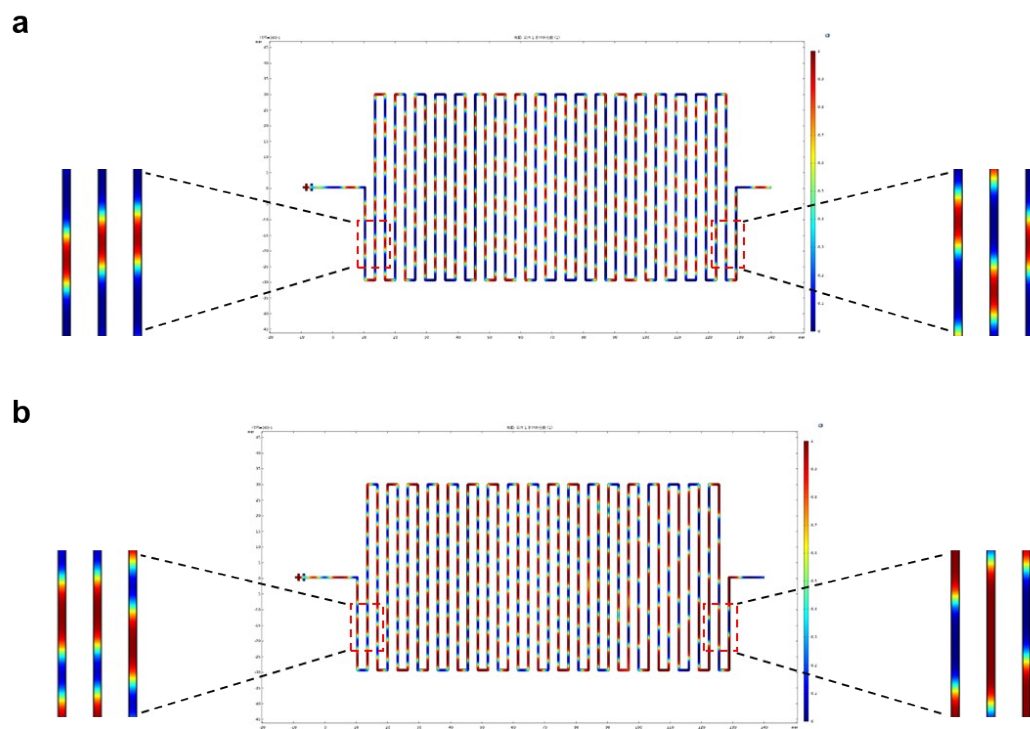


Figure S3. The zoom-in images for Figure 1c (ii) and (iii).

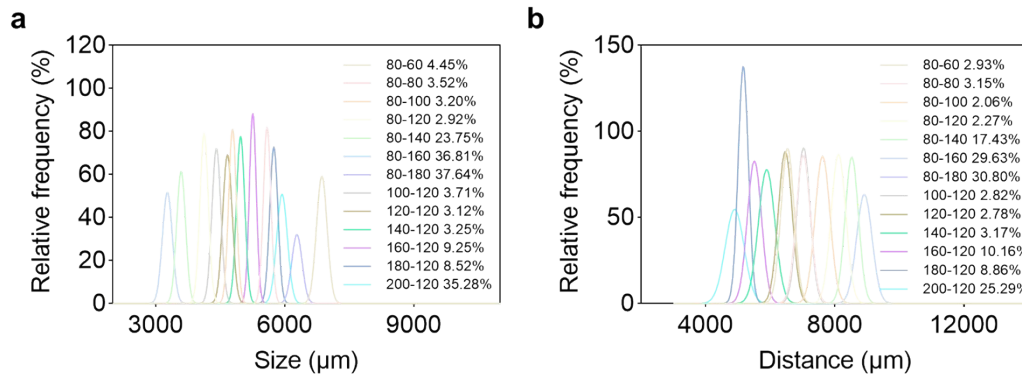


Figure S4. The distribution of the droplet size (a) and distance between the adjacent droplets (b) under varying flow rates. The values before and after the hyphen represent the total flow rate of aqueous phase and the flow rate of oil phase, respectively. The corresponding coefficient of variations (CVs) were indicated as well.

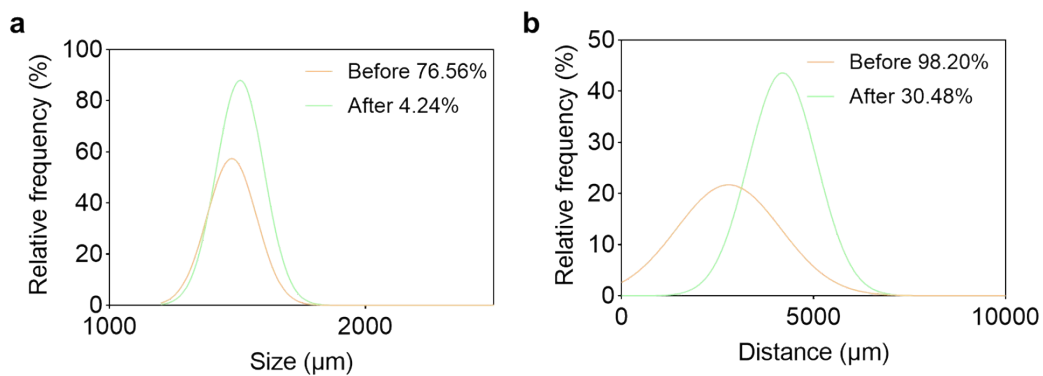


Figure S5. The distribution of the droplet size (a) and distance between the adjacent droplets (b) before and after enlargement of the outlet, where the total flow rate of aqueous phase and the flow rate of oil phase were $80 \mu\text{L min}^{-1}$ and $140 \mu\text{L min}^{-1}$, respectively. The corresponding CVs were indicated as well.

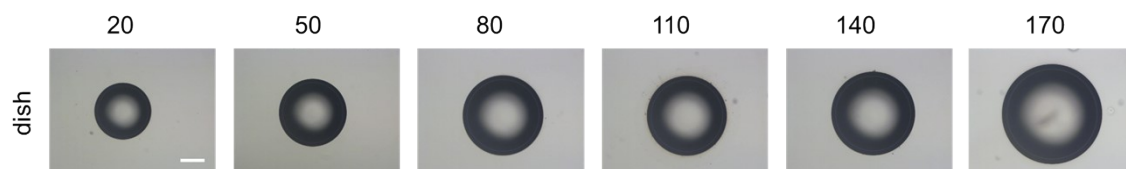


Figure S6. Bright-field images of the droplet collected in the Petri dish under varying flow rate of aqueous phase (20 $\mu\text{L min}^{-1}$, 50 $\mu\text{L min}^{-1}$, 80 $\mu\text{L min}^{-1}$, 110 $\mu\text{L min}^{-1}$, 140 $\mu\text{L min}^{-1}$, 170 $\mu\text{L min}^{-1}$, respectively) with a constant oil phase flow rate of 200 $\mu\text{L min}^{-1}$. The scale bar is 300 μm .

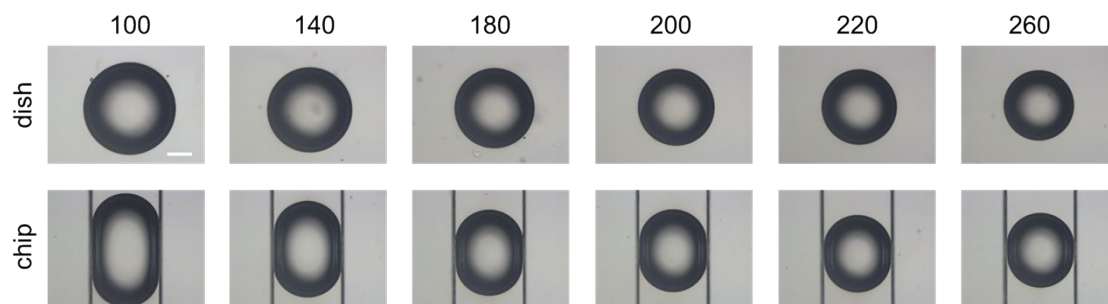


Figure S7. Representative microscopic images of droplets produced at different oil phase flow rates ($100 \mu\text{L min}^{-1}$, $140 \mu\text{L min}^{-1}$, $180 \mu\text{L min}^{-1}$, $200 \mu\text{L min}^{-1}$, $220 \mu\text{L min}^{-1}$, $260 \mu\text{L min}^{-1}$, respectively) with a constant aqueous phase flow rate of $80 \mu\text{L min}^{-1}$. The first row shows the bright field image of the droplet collected in the Petri dish, the second row displays the bright field image of the droplet on the chip. The scale bar was $300 \mu\text{m}$.

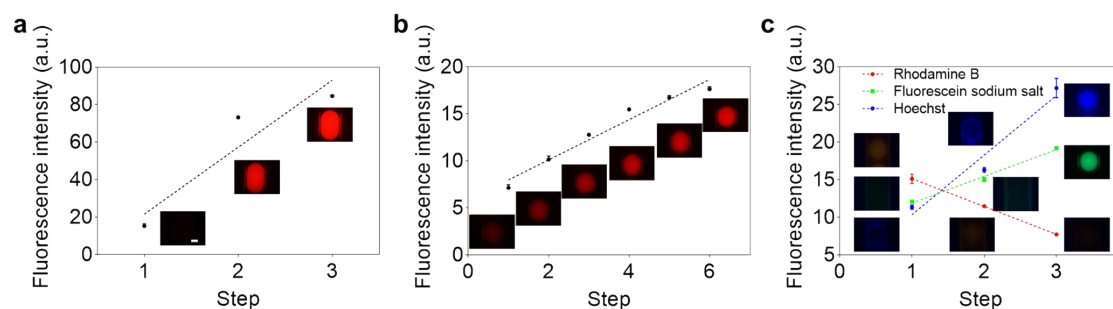


Figure S8. Tuning composition of droplets in a programmable way. (a) The average fluorescence intensity and representative fluorescence images of droplets under a 3-stepped loading scheme for a single drug. A simple linear regression was fitted to the data ($y = 35.710x - 14.11$, $R^2=0.8708$, $n=13$). (b) The average fluorescence intensity and representative fluorescence images of droplets under a 6-stepped loading scheme for a single drug. Simple linear regressions were fitted to the data ($y = 2.138x + 5.83$, $R^2=0.9241$, $n=13$). (c) The average fluorescence intensity and representative fluorescence images of droplets under a 3-stepped loading scheme for the combination of 3 types of drugs. Simple linear regressions were fitted to the data (blue fluorescence: $y = 7.925x + 2.42$, $R^2 = 0.8167$, $n=13$; red fluorescence: $y = -3.701x + 18.84$, $R^2 = 0.8361$, $n=13$; green fluorescence: $y = 3.555x + 8.33$, $R^2 = 0.9253$, $n=13$). The scale bar was $300 \mu\text{m}$.

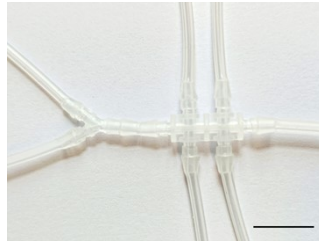


Figure S9. A representative photograph showing a seven-way valve assembled from a Y-shaped valve and a six-way valve. Scale bar: 10 mm.

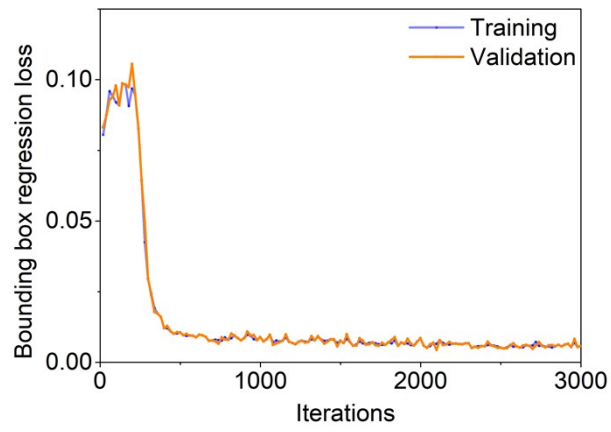


Figure S10. The bounding box regression loss curves for the training and validation data, respectively.

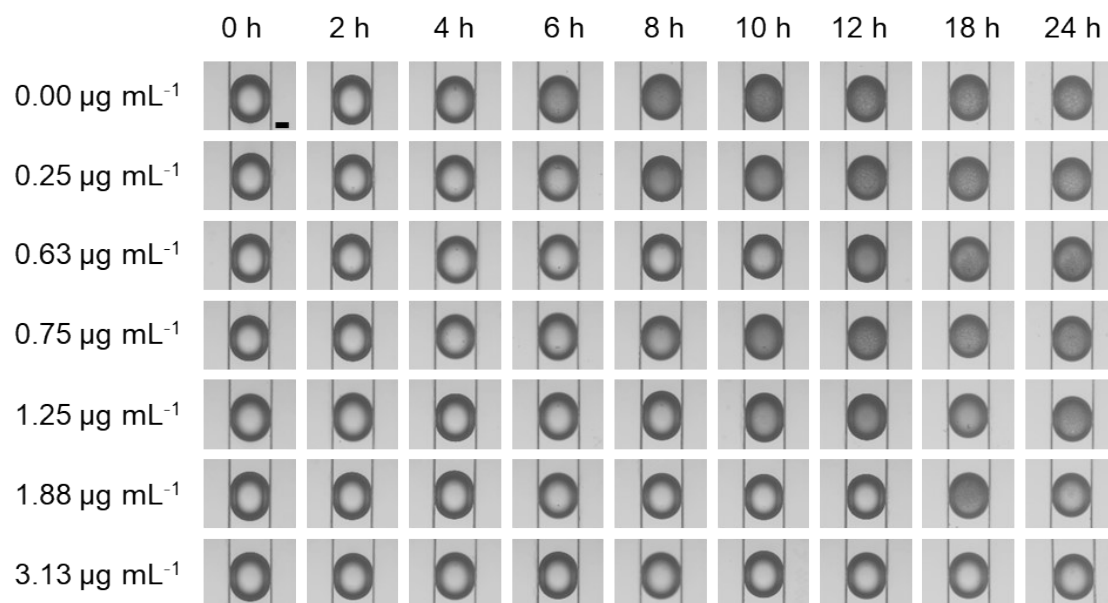


Figure S11. Representative bright-field images of the droplets containing *E. coli* exposed to chloramphenicol at multiple time points (0 h, 2 h, 4 h, 6 h, 8 h, 10 h, 12 h, 18 h, 24 h). The drug concentrations were 0.25 $\mu\text{g mL}^{-1}$, 0.63 $\mu\text{g mL}^{-1}$, 0.75 $\mu\text{g mL}^{-1}$, 1.25 $\mu\text{g mL}^{-1}$, 1.88 $\mu\text{g mL}^{-1}$, 3.13 $\mu\text{g mL}^{-1}$, respectively. The scale bar was 300 μm .

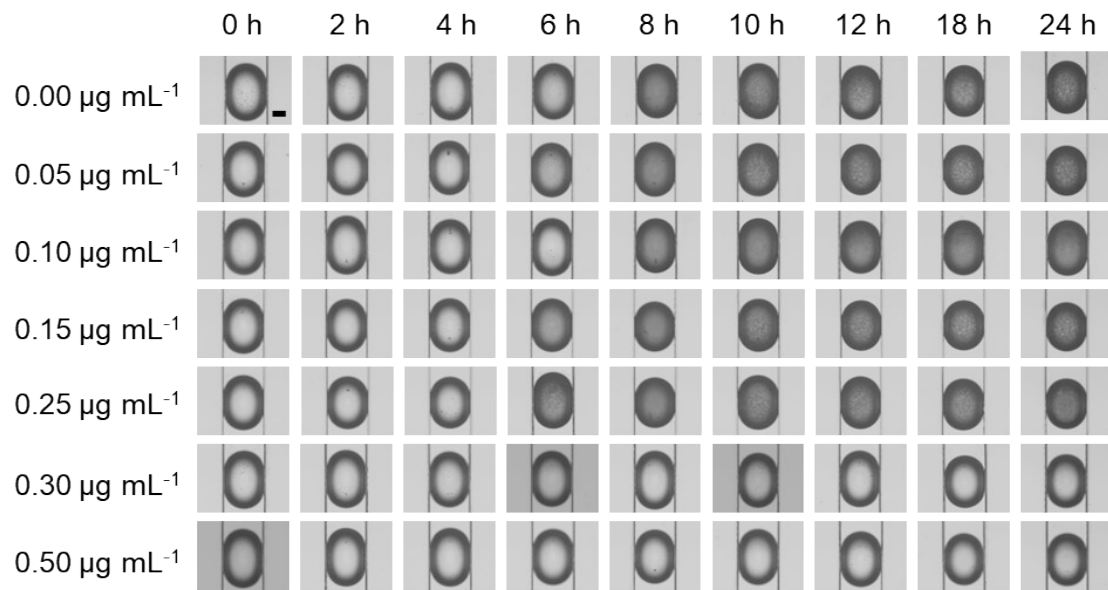


Figure S12. Representative bright-field images of the droplets containing *E. coli* exposed to tetracycline at multiple time points (0 h, 2 h, 4 h, 6 h, 8 h, 10 h, 12 h, 18 h, 24 h). The drug concentrations were 0.05 $\mu\text{g mL}^{-1}$, 0.10 $\mu\text{g mL}^{-1}$, 0.15 $\mu\text{g mL}^{-1}$, 0.25 $\mu\text{g mL}^{-1}$, 0.30 $\mu\text{g mL}^{-1}$ and 0.50 $\mu\text{g mL}^{-1}$, respectively. The scale bar was 300 μm .

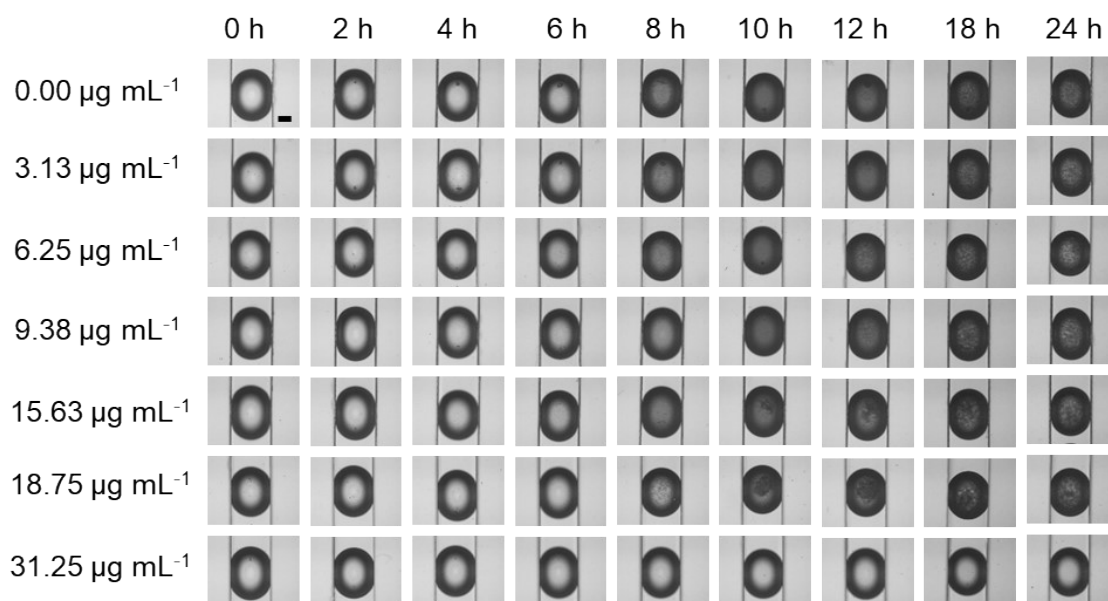


Figure S13. Representative bright-field images of the droplets containing *E. coli* exposed to cefepime at multiple time points (0 h, 2 h, 4 h, 6 h, 8 h, 10 h, 12 h, 18 h, 24 h). The drug concentrations were 3.13 $\mu\text{g mL}^{-1}$, 6.25 $\mu\text{g mL}^{-1}$, 9.38 $\mu\text{g mL}^{-1}$, 15.63 $\mu\text{g mL}^{-1}$, 18.75 $\mu\text{g mL}^{-1}$ and 31.25 $\mu\text{g mL}^{-1}$, respectively. The scale bar was 300 μm .

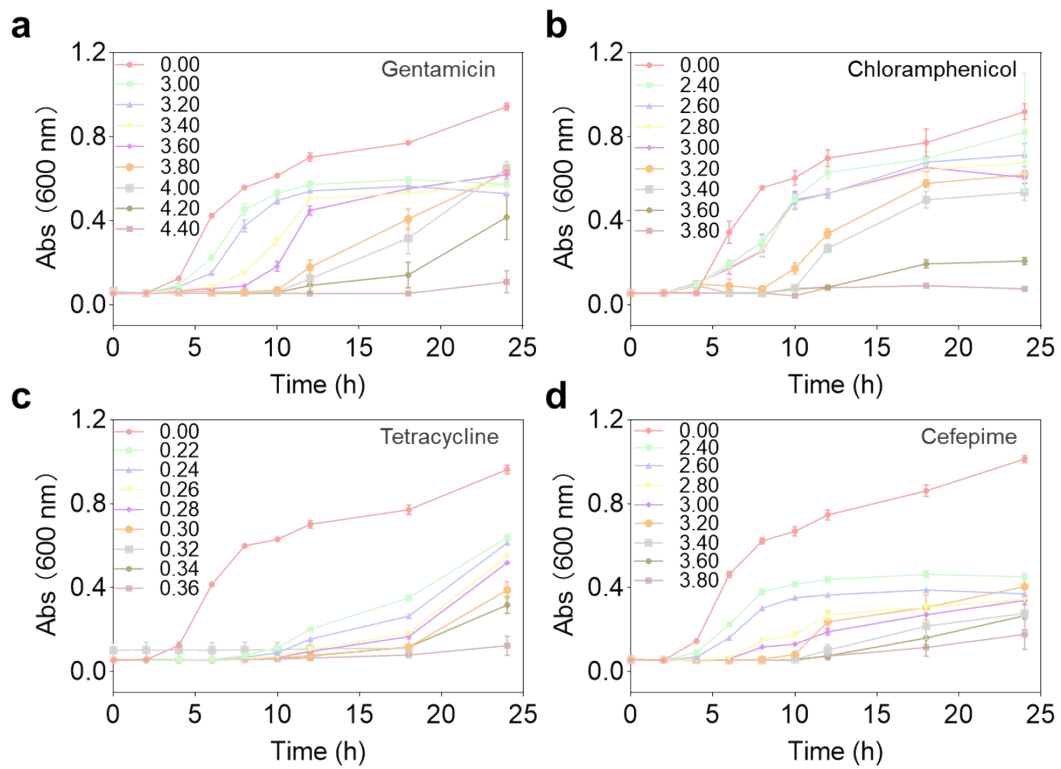


Figure S14. Plots showing the time-lapse change of absorbance (Abs) value of *E. coli* in well plates under treatment of different single antibiotics. (a) gentamicin; (b) chloramphenicol; (c) tetracycline and (d) cefepime. n=8.

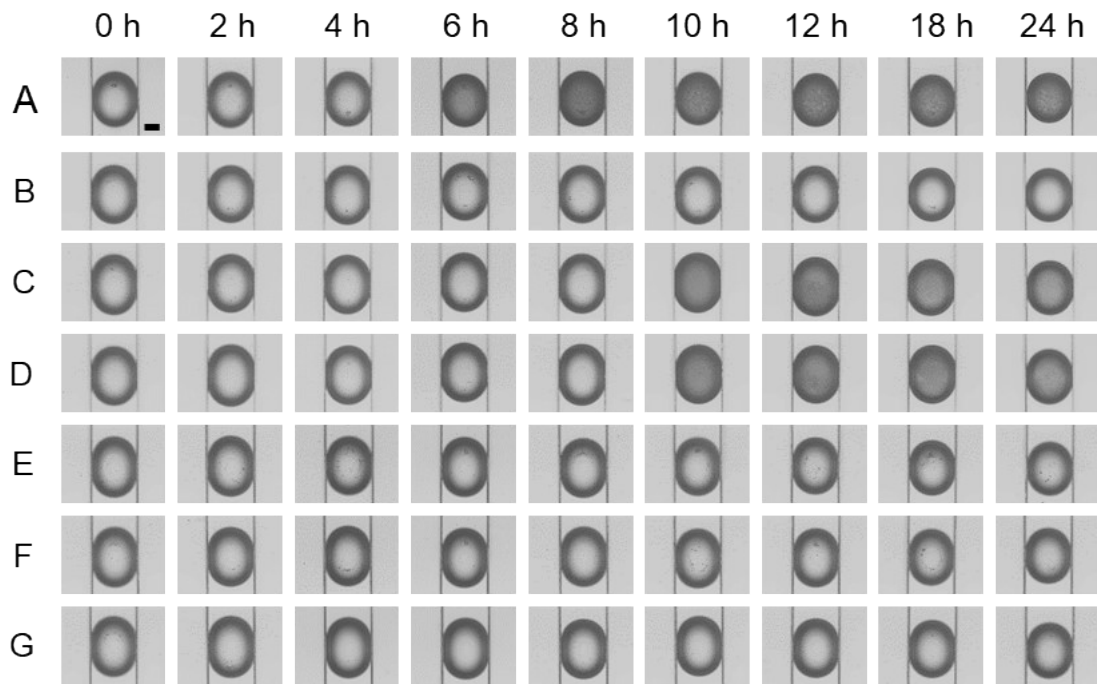


Figure S15. Representative bright-field images of the droplets containing *E. coli* exposed to gentamicin/tetracycline at multiple time points (0 h, 2 h, 4 h, 6 h, 8 h, 10 h, 12 h, 18 h, 24 h). The concentrations of drug combinations A-G were $0.00 \mu\text{g mL}^{-1}/0.00 \mu\text{g mL}^{-1}$, $0.25 \mu\text{g mL}^{-1}/0.17 \mu\text{g mL}^{-1}$, $0.75 \mu\text{g mL}^{-1}/0.10 \mu\text{g mL}^{-1}$, $1.25 \mu\text{g mL}^{-1}/0.03 \mu\text{g mL}^{-1}$, $0.38 \mu\text{g mL}^{-1}/0.25 \mu\text{g mL}^{-1}$, $1.13 \mu\text{g mL}^{-1}/0.15 \mu\text{g mL}^{-1}$ and $1.88 \mu\text{g mL}^{-1}/0.05 \mu\text{g mL}^{-1}$, respectively. The scale bar is $300 \mu\text{m}$.

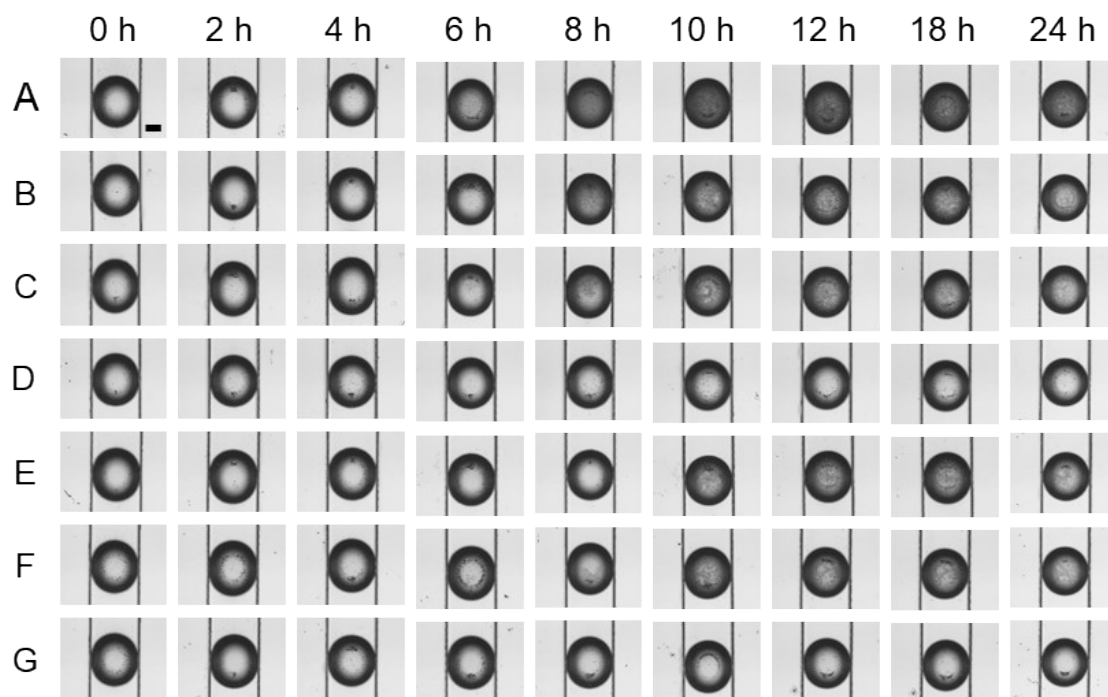


Figure S16. Representative bright-field images of the droplets containing *E. coli* exposed to gentamicin/cefepime at multiple time points (0 h, 2 h, 4 h, 6 h, 8 h, 10 h, 12 h, 18 h, 24 h). The concentrations of drug combinations A-G were $0.00 \mu\text{g mL}^{-1}/0.00 \text{ ng mL}^{-1}$, $0.38 \mu\text{g mL}^{-1}/15.63 \text{ ng mL}^{-1}$, $1.13 \mu\text{g mL}^{-1}/9.38 \text{ ng mL}^{-1}$, $1.88 \mu\text{g mL}^{-1}/3.13 \text{ ng mL}^{-1}$, $0.50 \mu\text{g mL}^{-1}/20.63 \text{ ng mL}^{-1}$, $1.50 \mu\text{g mL}^{-1}/12.38 \text{ ng mL}^{-1}$ and $2.50 \mu\text{g mL}^{-1}/4.13 \text{ ng mL}^{-1}$, respectively. The scale bar is 300 μm .

Supporting Tables

Table S1. The dimensions of the microliter-droplet channel

Type	Width of the channel (mm)	Height of the channel (mm)	Inner radius of the channel corner (mm)	Outer radius of the channel corner (mm)
Designed value	0.70	0.70	0.30	0.50
Actual value	0.96 ± 0.01	1.01 ± 0.01	0.20 ± 0.00	0.60 ± 0.03

Table S2. The dimensions of the droplet generator

Diameter of orifice (mm)	Diameter of inner channel (mm)	Minimum outer diameter of inlet (mm)	Maximum outer diameter of inlet (mm)
1.06	1.06	1.70	2.78

Table S3. The loading scheme to optimize the flow rate of aqueous phase

Step	Flow rate of the total aqueous phase ($\mu\text{L min}^{-1}$)	Flow rate of the oil phase ($\mu\text{L min}^{-1}$)
1	20	200
2	50	200
3	80	200
4	110	200
5	140	200
6	170	200

Table S4. The loading scheme to optimize the flow rate of oil phase

Step	Flow rate of the total aqueous phase ($\mu\text{L min}^{-1}$)	Flow rate of the oil phase ($\mu\text{L min}^{-1}$)
1	80	100
2	80	120
3	80	140
4	80	160
5	80	180
6	80	200
7	80	220
8	80	240
9	80	260

Table S5. The 3-stepped loading scheme.

Step	Inlet 1 ($\mu\text{L min}^{-1}$)	Inlet 2 ($\mu\text{L min}^{-1}$) 1)	Inlet 3 ($\mu\text{L min}^{-1}$) 1)	Inlet 4 ($\mu\text{L min}^{-1}$) 1)	Inlet 5 ($\mu\text{L min}^{-1}$) 1)
1	20	10	50	200	200
2	20	30	30	200	200
3	20	50	10	200	200

Table S6. The 5-stepped loading scheme.

Step	Inlet 1 ($\mu\text{L min}^{-1}$)	Inlet 2 ($\mu\text{L min}^{-1}$) 1)	Inlet 3 ($\mu\text{L min}^{-1}$) 1)	Inlet 4 ($\mu\text{L min}^{-1}$) 1)	Inlet 5 ($\mu\text{L min}^{-1}$) 1)
1	20	10	50	200	200
2	20	20	40	200	200
3	20	30	30	200	200
4	20	40	20	200	200
5	20	50	10	200	200

Table S7. The 6-stepped loading scheme.

Step	Inlet 1 ($\mu\text{L min}^{-1}$)	Inlet 2 ($\mu\text{L min}^{-1}$) 1)	Inlet 3 ($\mu\text{L min}^{-1}$) 1)	Inlet 4 ($\mu\text{L min}^{-1}$) 1)	Inlet 5 ($\mu\text{L min}^{-1}$) 1)
1	20	10	50	200	200
2	20	20	40	200	200
3	20	30	30	200	200
4	20	40	20	200	200
5	20	50	10	200	200
6	20	60	0	200	200

Table S8. The 3-stepped loading scheme for the combination of three types of fluorescence dyes.

Step	Inlet 1 ($\mu\text{L min}^{-1}$)	Inlet 2 ($\mu\text{L min}^{-1}$)	Inlet 3 ($\mu\text{L min}^{-1}$)	Inlet 4 ($\mu\text{L min}^{-1}$)	Inlet 5 ($\mu\text{L min}^{-1}$)	Inlet 6 ($\mu\text{L min}^{-1}$)
1	10	10	10	50	200	200
2	10	20	20	30	200	200
3	10	30	30	10	200	200